can be fulfilled if $\bar{\alpha}_{-\infty}$ is sufficiently small compared to unity. Then it follows that the terms on the right-hand side of Eq. (C2) also can be omitted, since the ratios of those to $\rho_o(\mathbf{U}_o \cdot \nabla)\tilde{\mathbf{u}}$ on the left-hand side are at most of order $\bar{\alpha}_{-\infty}$. Similar estimation can be made for the continuity and energy equations, too. Consequently we can reach the linearized steady and unsteady equations of acoustic type adopted in the text.

Finally, it remains to consider the order of magnitude of the unsteady body force $\tilde{\mathbf{F}}$ which is composed of the effect of the unsteady lift force and the effect of the blade displacement with finite lift force. We denote the former by $\tilde{\mathbf{F}}_d$ and the latter by $\tilde{\mathbf{F}}_q$. Then we can estimate them as follows

$$\tilde{\mathbf{F}}_d \sim \rho_o U_o a^* \omega/c, \quad \tilde{\mathbf{F}}_q \sim \rho_o U_o^2 \bar{\alpha}_{-\infty} a^*/c^2$$

Therefore $\tilde{\mathbf{F}}_q/\tilde{\mathbf{F}}_d \sim \bar{\alpha}_{-\infty}/(\omega c/U_o)$. Here c denotes the blade chord. We see that $\tilde{\mathbf{F}}_q$ is of the same order as $\tilde{\mathbf{F}}_d$ if the reduced frequency $\omega c/U_o$ is of the same order as $\bar{\alpha}_{-\infty}$.

To conclude, the perturbation adopted in the text is rational when $\bar{\alpha}_{-\infty}$ is small and at the same time the reduced frequency is as small as $\bar{\alpha}_{-\infty}$.

References

[1] Shiori, J., "Non-stall Normal Mode Flutter in Annular Cascade, Part I, Theoretical Study," *Transactions of the Japan Society of Aeronautical Engineering*, Vol. 1, Nov. 1958, pp. 26–35.

[2] Whitehead, D. S., "Bending Flutter of Unstalled Cascade Blades at Finite Deflection," R & M 3386, Oct. 1965, British Aeronautical Research Council, London, Eng.

[3] Hanamura, Y. and Tanaka, H., "The Flexure-Torsion Flutter of Aerofoils in Cascade, 1st Rep., Computation and Experiment of Unsteady Aerodynamic Derivatives," *Bulletin of the Japan Society of Mechanical Engineers*, Vol. 10, No. 40, Aug. 1967, pp. 647–662.

[4] Lane, F. and Friedman, M., "Theoretical Investigation of Subsonic Oscillatory Blade-Row Aerodynamics," TN 4136, 1958, NACA.

[5] Whitehead, D. S., "Vibration and Sound Generation in a Cascade of Flat Plates in Subsonic Flow," R & M 3685, Feb. 1970, British Aeronautical Research Council, London, Eng.

[6] Smith, S. N., "Discrete Frequency Sound Generation in Axial Flow Turbomachines," R & M 3709, 1973, British Aeronautical Research Council, London, Eng.

[7] Kaji, S. and Okazaki, T., "Cascade Flutter in Compressible Flow" (in Japanese), *Transactions of Japan Society of Mechanical Engineers*, Vol. 38, No. 309, May 1972, pp. 1023–1033.

[8] Nishiyama, T. and Kobayashi, H., "Theoretical Analysis for Unsteady Characteristics of Oscillating Cascade Aerofoils in Subsonic Flows," Technology Reports, Tohoku Univ., Vol. 38, No. 1, July 1973, pp. 287–314.

[9] Kaji, S. and Okazaki, T., "Propagation of Sound Waves Through a Blade Row, II. Analysis Based on the Acceleration Potential Method," *Journal of Sound and Vibrations*, Vol. 11, March 1970, pp. 355–375.

[10] Lighthill, M. J., *Introduction to Fourier Analysis and Generalised Functions*, Cambridge Univ. Press, Cambridge, Eng., 1964, pp. 67–68.

MAY 1975 AIAA JOURNAL VOL. 13, NO. 5

Screen Nozzles for Gasdynamic Lasers

DAVID A. RUSSELL,* STANFORD E. NEICE,† AND PETER H. ROSE‡

Mathematical Sciences Northwest, Inc., Seattle, Wash.

Fine-hole orifice plates (screen nozzles) are considered as a replacement for two-dimensional grid nozzles in gasdynamic lasers. Analyses are made of the downstream fully mixed state, the flow perturbation decay to that state, and the optical gain distribution for typical N_2-CO_2 laser conditions. Experiments were conducted with a screen nozzle mounted on a shock tube. Density nonuniformities were found to be below 1% at 100 orifice spacings downstream (30 cm), with gains of 0.6–0.8%/cm. These results agree with predictions and lead to the conclusion that screen nozzles offer extreme simplicity with only small performance penalty.

I. Introduction

A HIGH degree of flow uniformity is required in the cavity of a modern gasdynamic laser (GDL) if significant distortion of the extracted beam is to be avoided. This has led to considerable study of the aerodynamic details of the flow. A review of some of this work[1] points out that GDL grid nozzles must be designed by the method-of-characteristics and must have carefully selected entrance profiles,[2] contoured and flat-wall boundary-layer corrections,[3] and nozzle trailing edge truncation compromising conflicting requirements of strength and flow uniformity.[4] Further, high operating pressure levels lead directly to small nozzle scales (0.01–0.02 cm throat height), and to machining and assembly tolerances that are difficult and costly to meet.

The present paper considers the feasibility of replacing the standard array of these nozzles with an orifice plate containing simple drilled holes of specified geometry and size. From strictly dimensional reasoning, the disturbance level due to the nonideal nature of the orifice flow would be expected to decay with a downstream distance measured in terms of the characteristic orifice spacing. Thus, with a sufficiently fine scale "screen nozzle," it should be possible to achieve adequate flow uniformity at a distance downstream that is still acceptable for the nonequilibrium aspects of a GDL.

Earlier studies of screen nozzles for supersonic wind tunnels[5] identified nonideal features of the downstream flow. These were waves arising from impingement of the jets from adjacent nozzles, the wake structure, and waves originating at the duct walls. The present study considers disturbances in the body of the flow in more detail, with emphasis on the N_2-CO_2 GDL

Presented as Paper 74-549 at the AIAA 7th Fluid and Plasma Dynamics Conference, Palo Alto, Calif., June 17–19, 1974; submitted July 1, 1974; revision received October 29, 1974. This work was supported by the United States Air Force Systems Command (AFWL) under Contract F29601-73-A-0039. The authors wish to thank E. Braunschweig of AFWL for initiating this project, and R. V. Hemm, B. Masson, R. A. Tennant, and W. B. Watkins at that laboratory for helpful comments. J. F. Newton of MSNW performed the experiments to be discussed, while A. L. Pindroh carried out many of the calculations. Some of the first author's contributions were made possible through Grant AFOSR 73-2512 at the University of Washington.

Index categories: Lasers; Jets, Wakes, and Viscid-Inviscid Flow Interactions; Nozzle and Channel Flows.

* Consultant. Professor, Department of Aeronautics and Astronautics, University of Washington. Associate Fellow AIAA.

† Senior Engineer. Member AIAA.

‡ President. Associate Fellow AIAA.

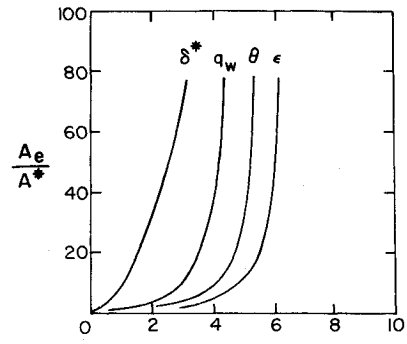

Fig. 1 Integral boundary-layer parameters (conical nozzles; T_o = 2000 K; T_w = 300 K; N_2). $(\delta^*/d)_e(p_o d^* \sin a)^{1/2} \times 10^2 \sim (\text{atm-cm})^{1/2}$. $(\theta/d)_e(p_o d^* \sin a)^{1/2} \times 10^3 \sim (\text{atm-cm})^{1/2}$. $-(\varepsilon/d)_e(p_o d^* \sin a)^{1/2} \times 10^3 \sim (\text{atm-cm})^{1/2}$. $q_w(p_o d^{*3}/\sin a)^{-1/2} \times 10^{-2} \sim W/(\text{atm-cm}^3)^{1/2}$.

application. Cavity wall boundary-layer effects are generally ignored, these being common to any laser and correctable by careful wall contouring.

The screen nozzle is analyzed in the next section. The nozzle expansion and the downstream uniformly mixed flow are first considered, followed by a discussion of the approach to that final mixed state, and calculations of the optical gain expected with various assumptions for the rate of mixing. An experimental program was undertaken to support and extend the analyses. This involved testing a screen nozzle under a variety of conditions on a shock tube. The downstream Mach number, density perturbation level, and gain were studied by shadowgraph, interferometric, and CO_2 probe laser techniques, respectively. These experiments are described in Sec. III, while Sec. IV discusses the results. Conclusions are offered.

II. Analysis

A. Screen Nozzle Expansion

The main feature of the individual screen nozzle orifices is the axisymmetric supersonic expansion. For the same throat height (d^*) and area ratio (A_e/A^*), the exit dimension (d_e) of an axisymmetric nozzle is reduced by $(A_e/A^*)^{1/2}$ over that of a 2-D nozzle. There is also a considerable reduction in nozzle length between 3-D[6] and 2-D minimum length contoured nozzles. However, flow property gradients near the throat where the vibrational freezing is to occur are quite similar in the two cases, the three-dimensionality of the axisymmetric expansion being balanced by the more rapid wall divergence of the 2-D nozzle. Further, for $A_e/A^* = 60$ with $\gamma = 1.4$, it turns out that a simple conical nozzle with a 10° half angle has comparable throat gradients, and is an additional 40% shorter in over-all length than the 3-D minimum length nozzle.

The laminar boundary layers in the various nozzles were calculated using integral techniques.[7] Results for conical nozzles with arbitrary half angles (α) are shown on Fig. 1. Here A_e/A^* is plotted vs boundary-layer integral properties for ideal 1-D, N_2 flow with the Prandtl number taken to be unity. Representative values of total temperature (T_o) and wall temperature (T_w) were chosen as 2000 K and 300 K, respectively; decreasing T_o or increasing T_w has the effect of reducing all of the abscissa values. The displacement thickness (δ^*), momentum thickness (θ), and total enthalpy flux thickness (ε) evaluated at the nozzle exit are shown on the figure. They have been normalized by dividing by d_e, while the parameter $(p_o d^* \sin \alpha)^{1/2}$ provides the basic pressure-length scale dependence that characterizes laminar flow. The total integrated heat transfer to the nozzle walls is also presented in Fig. 1. The magnitude of this parameter will show that, although water cooling passages are necessary for continuous lasers, the problems associated with cooling screen nozzles are not particularly difficult to meet. While the boundary layers on contoured nozzles were individually calculated in the present study, the exit thicknesses may be approximated from Fig. 1 by using an effective throat-to-exit value of α.

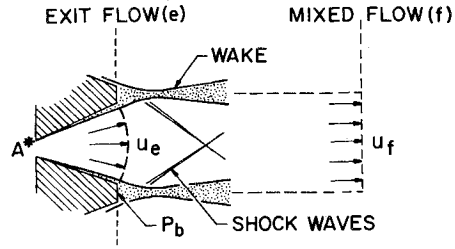

Fig. 2 Model for determining properties of the fully mixed flow.

B. Properties of the Fully Mixed Flow

The flow in the immediate vicinity of a screen nozzle orifice is depicted in Fig. 2. The nozzle boundary layers are shown feeding the wakes, and the start of a repetitive shock pattern is seen to occur as the supersonic flow from the orifice is forced to turn. In the absence of further perturbing influences, the resulting complex flow must eventually dissipate to a uniform parallel state. By symmetry, there is no net momentum or energy transfer across the wake centerlines from adjacent orifice flows. Thus, the mixed state can be found by solving conservation equations written between the nozzle exit and far downstream, without having to specify the flow processes in between.

The core exit flow may be approximated as uniform and conical with specified angle (α), where α is equal to the cone half angle for conical nozzles but approaches zero for contoured ones. Assuming further that the boundary layer at the exit plane is thin relative to d_e (see Fig. 1), the conservative equations may be written in integral form and evaluated for the present geometry to yield

$$\rho_e u_e[2(1+\cos\alpha)^{-1} - 4(\delta^*/d)_e] \approx \rho_f u_f (A_f/A_e)$$

$$p_e[1 + p_b/p_e(A_f/A_e - 1)] + \rho_e u_e^2[1 - 4(\delta^*/d)_e \cos\alpha - 4(\theta/d)_e \cos\alpha] \approx p_f + \rho_f u_f^2 (A_f/A_e) \quad (1)$$

$$\rho_e u_e T_{oe}[2(1+\cos\alpha)^{-1} - 4(\delta^*/\theta)_e - 4(\varepsilon/d)_e] \approx \rho_f u_f T_{of}(A_f/A_e)$$

Here subscript e refers to the nozzle exit flow, while f refers to the final mixed state. Plane cross-sectional area ratios are used. The base pressure (p_b) must be specified when $A_f/A_e \neq 1$. Although p_b/p_e will probably be slightly less than unity, a precise value would have to come from experiment.

With the exit flow specified, Eqs. (1) may be solved with the perfect gas relation to obtain a closed form expression for M_f and the other mixed state properties. Results are shown in Fig. 3 for $A_e/A^* = 60$ conical nozzles with $A_f = A_e$ and boundary-layer inputs from Fig. 1. $p_o d^*$ is used as the abscissa, with α as a parameter. Shock losses dominate over boundary-layer effects for large α, resulting in a reduced $p_o d^*$ dependence. On the other hand, small α produces a weak shock system but severe boundary-layer losses at low $p_o d^*$. Conventional GDLs operate with

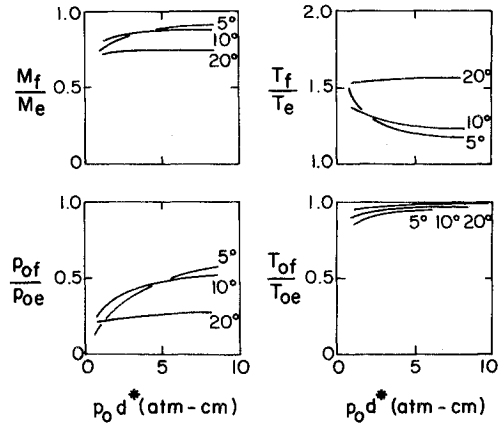

Fig. 3 Results of mixing analysis ($A_f/A_e = 1$; $A_e/A^* = 60$ conical nozzles; boundary-layer inputs from Fig. 1).

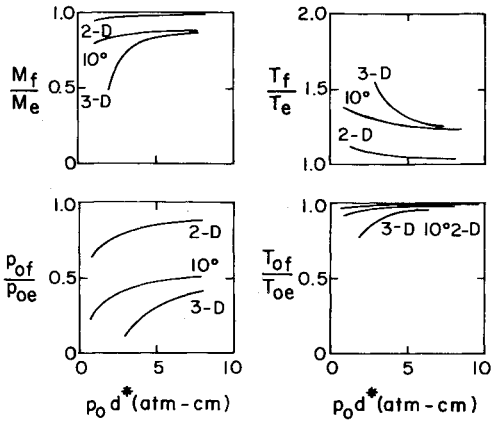

Fig. 4 Results of mixing analysis ($A_f/A_e = 1$; $A_e/A^* = 60$ minimum length contoured and 10° conical nozzles; $T_o = 2000$ K; $T_w = 300$ K; N_2).

$p_o d^* \approx 1$ atm cm. Figure 3 suggests that selection of $\alpha = 10°$ would minimize the changes in M, p_o, and T that occur as a result of mixing at this $p_o d^*$.

Figure 4 compares mixing analysis results for 10° conical nozzles with 3-D and 2-D minimum length contoured nozzles. A practical nozzle wall truncation angle[4] of 2° was assumed for the contoured nozzles; however, shock losses for these nozzles turn out to be negligible compared with losses due to the boundary layers. This figure shows that the 3-D nozzle has much more serious boundary-layer effects than the 2-D one. Although the 2-D contour is longer, the boundary layer occupies a smaller fraction of the exit area, hence accounting for the performance differences. It is seen that the reduced length of the 10° cone results in a considerable decrease in losses over the 3-D case.

The p_o losses of the 10° conical nozzle relative to the 2-D nozzle are not as serious a problem as would first appear from Fig. 4. This figure shows a small relative decrease in M_f accompanying the p_o loss. Thus, a fixed throat diffuser with a total pressure loss equivalent to that of a normal shock at M_f would produce less loss in the 10° case. Comparing $A_e/A^* = 60$ systems at $\gamma = 1.4$, the over-all pressure recovery ratio for the 10° case turns out to be ≈85% of that for the 2-D when both are operated at $p_o d^* \approx 1$. Moreover, Sec. IV B will reveal that screen nozzles should be operated at higher $p_o d^*$, further reducing the comparative p_o loss and giving the screen nozzle system better pressure recovery in some instances.

C. Decay of Density Perturbations

While a complete solution of the flowfield between the screen nozzle exit and the final mixed state is impracticable, some understanding can be achieved by considering simple models for the essential fluid flow features. The nozzle boundary layers feed the wakes (Fig. 2), which have unstable profiles and quickly become turbulent, spreading the momentum and energy defects throughout the fluid. The complex initial geometry of the wake system may be assumed to ultimately take the form of an array of axisymmetric wakes, with centerline spacing equal to the orifice spacing (d_s). With the momentum defect of a single nozzle appearing in each wake, it can be shown that the frictional drag coefficient times cross-sectional area of an equivalent wake producing body is equal to $2\pi\theta_e d_s$. The mixing-length-model similar solution of the turbulent boundary layer equations then gives[8]

$$\frac{u_\infty - u}{u_\infty} = 2\pi \frac{(\theta_e/d_s)^{1/3}}{(x/d_s)^{2/3}} \left[\frac{(\tilde{r}/d_s)^{3/2}}{3[2\pi\theta_e/d_s(x/d_s)]^{1/2}} - 0.42(b/l)^{0.315} \right]^2 \quad (2)$$

for the axisymmetric wake velocity perturbation. Here b is the half width from a wake centerline to where $u_\infty - u = 0$. The mixing length (l) is assumed to be constant over b. The quantity b/l comes from experiment: it will be taken to have a value of 5, in approximate agreement with incompressible 2-D wake results.[9]

Although Eq. (2) was developed for incompressible flow, it has here been extended to the compressible case by replacing the transverse coordinate (r) by $\tilde{r} = \int_0^r \rho/\rho_\infty \, dr$, where ρ_∞ refers to the local freestream density external to the wake. Flows of present interest have a relatively small density difference across the boundary layer at the nozzle exit, and this difference decreases downstream. Thus, $\tilde{r} = r$ to a good approximation. The maximum velocity nonuniformity at a given x location is then given by taking the difference between Eq. (2) evaluated at $\tilde{r} = 0$ and at $\tilde{r} = d_s/2$.

The maximum density perturbation may be related to the velocity perturbation by assuming a temperature profile that is similar in form to the $u(r)$ profile, and utilizing the fact that both θ and ε must remain constant downstream of the nozzle. With the further assumption that the temperature wake width is equal to the inverse square root of the turbulent Prandtl number (Pr_t) times the velocity width, the expression

$$\frac{\Delta\rho}{\rho_\infty} \approx Pr_t^{1/2} \frac{2(1 - T_\infty/T_o) - (\varepsilon/\theta)_e}{T_\infty/T_o} \frac{\Delta u}{u_\infty} \quad (3)$$

can be obtained for 2-D wakes.[10] Equation (3) gives values of $(\Delta\rho/\rho_\infty)(\Delta u/u_\infty)^{-1}$ for present conditions of interest ≈4. This has been used with Eq. (2) to obtain one of the density perturbation decay curves of Fig. 5, for a representative value of θ_e/d_s of 10^{-2} (see Fig. 1). It should be noted that adjacent wakes begin to merge soon after leaving the orifice plate, and the superposition effect would be expected to reduce $\Delta\rho/\rho_\infty$ further. Integration along a beam path also reduces the effective density perturbation. Thus, the curve should be regarded as an upper limit for wake disturbances.

The shock pattern also contributes to local density disturbances. An analysis of this effect for 2-D flows[4] gives the maximum density perturbation at fixed downstream distance as

$$\frac{\Delta\rho}{\rho_f} = \frac{2}{\gamma+1} M_f \left(\frac{x}{d_s}\right)^{-1} \quad (4)$$

for $M_f^2 \gg 1$ and $[(\gamma+1)/2](x/d_s)(\theta/d_s) \gg 1$. Equation (4) is plotted in Fig. 5 for $M_f = 6$. This curve must also be regarded as a maximum as there should be 3-D relief. Furthermore, there is an integrated path cancelling effect if the wave pattern is regular. It is then only the x-dependence difference over the characteristic pattern length of $(M_f^2 - 1)^{1/2} d_s/2$ that becomes important, and the average local disturbance can be shown to reduce to[4]

$$\frac{\Delta\rho}{\rho_f} \approx \frac{\gamma - 1}{\gamma(\gamma+1)^2} \left(\frac{x}{d_s}\right)^{-2} \quad (5)$$

This gives a disturbance level (Fig. 5) that is many orders of magnitude below the other predictions. Such a low wave contribution would require extreme pattern regularity and

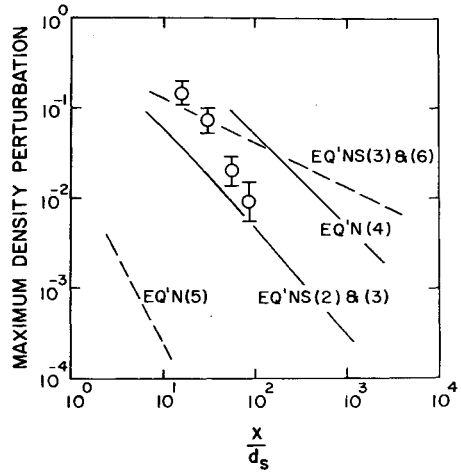

Fig. 5 Models for maximum density perturbation decay (data discussed in Sec. IVA).

precise wall boundary layer cancellation. Although this is unlikely, Eq. (5) does give an indication of the large canceling effects that are possible with regular density patterns.

There will in general be time varying random density fluctuations superimposed on the mean profiles just discussed. For turbulent wakes it might be expected that $\rho'_{rms}/\Delta\rho \approx u'_{rms}/\Delta u \approx (l/\Delta u)\,du/dy = 0\,(l/d_s)$ after wake merging. With $(b/l) = 5$, and the turbulence integral scale (Λ) approximately equal to the mixing length, $\Lambda/d_s = 0(10)^{-1}$ and $\rho'_{rms}/\Delta\rho = 0(10)^{-1}$. If the flow patterns just discussed are not completely regular, there may be an effective ρ'_{rms} of $\Delta\rho$, while Λ may increase to d_s, $(M_f{}^2-1)^{1/2}d_s/2$, or even larger if multi-jet instabilities occur. Indeed, in the absence of further downstream inputs, the flow might ultimately take on the character of an isotropic turbulence field. Classical grid turbulence has[11]

$$\frac{u'_{rms}}{u_\infty} \approx C\left(\frac{x}{d_s}\right)^{-1/2} \tag{6}$$

where the constant of proportionality primarily involves the initial momentum defect. Applying this expression to compressible flow and using the appropriate form of Eq. (3) gives an expression for ρ'_{rms}/ρ_∞. This is shown on Fig. 5 for an incompressible low-blockage screen flow C of 10^{-1}. While little is known about the actual value of C and the effective origin of x for screen nozzles, in the absence of wall effects the density perturbation decay is eventually expected to take on the slow $x^{-1/2}$ dependence indicated on the figure.

D. Gain Calculations

Standard four-temperature-model nonequilibrium calculations[12] were performed for a laser gas consisting of 89% N_2, 10% CO_2, and 1% H_2O by volume. The calculations were carried along the nozzle centerlines and into the cavities. Figure 6 shows the resulting gain vs distance from the nozzle exit plane for $A_e/A^* = 60$, 2-D and 10° conical nozzles. T_o was chosen as 2000 K with $p_o d^* = 0.8$ atm cm and $d^* = 0.015$ cm. The dashed lines are for no viscous losses. As expected (Sec. II. A.) these show little difference in nozzle performance. On the other hand, the solid curves of Fig. 6 result if the nozzle exit flow is assumed to jump immediately to the final mixed state (see Fig. 4).

The models of Sec. IIC generally predict that it takes a downstream distance of $0(10)^2$ d_s for mixing to progress to the point where density disturbances have decayed to $(10)^{-2}$ ρ_∞. Gain calculations were made assuming that the temperature change due to mixing occurs linearly over this distance. The gain was found to initially follow the inviscid calculation, subsequently falling off to slightly higher than the instantaneously mixed value at 100 d_s. The downstream agreement suggests that instantaneous mixing is a reasonable model to use for predicting screen nozzle mixed state performance. Indeed, the complexity

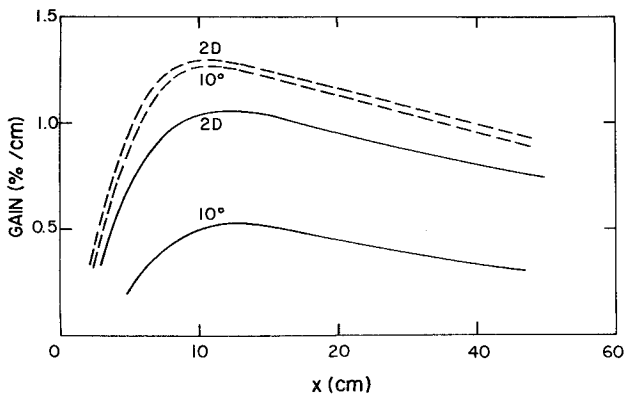

Fig. 6 Gain downstream of 2-D grid nozzle and 10° screen nozzle (dashed lines are no losses, solid lines for instantaneous mixing; $A_e/A^* = 60$; $T_o = 2000$ K; $T_w = 300$ K; $p_o d^* = 0.8$ atm-cm; $d^* = 0.015$ cm; 89% N_2 − 10% CO_2 − 1% H_2O).

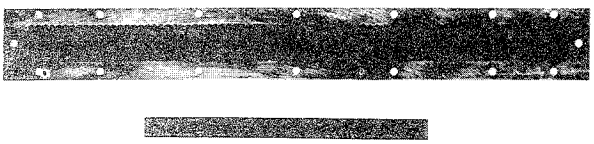

Fig. 7 Downstream face of screen nozzle.

and nonuniformity of the flow prior to this point makes use of more involved models questionable.

The flow from the 10° nozzle is thus expected to be essentially mixed for the right half of Fig. 6, and it can be seen that viscous effects have caused a substantial loss of gain. However, while the conventional 2-D nozzle performance is optimized with $p_o d^* = 0.8$ atm cm, the relatively high fluid mechanical losses that occur in screen nozzles dictate use of higher $p_o d^*$. For example, calculations show that the mixed flow gain of a screen nozzle at $p_o d^* = 2$ atm cm is increased to ≈70% of the 2-D value of Fig. 6. As would be expected from Fig. 4, the loss in gain for the 3-D contoured nozzle was much more severe for all practical values of $p_o d^*$. Consequently, that nozzle will not be considered further.

III. Experiment

A. Facility and Operating Conditions

A stainless steel shock tube supplied the gas flow for the experiments. This utilized simple pressure break diaphragms to separate a 4.8-m long 11.5-cm i.d. driver from an 8.5-m length of 7.5-cm i.d. driven tube. The driven tube was anchored to a massive concrete block in order to limit movement and thus facilitate low-noise-level gain measurements. A secondary diaphragm station was located at the tube's downstream end. This was followed by a two section transition to a 2 × 28-cm rectangular channel. The first section had a uniformly decreasing cross-sectional area from the 7.5 cm i.d. tube to a 1 × 28-cm cross section. This was followed by a short expansion in which the channel height was increased to 2 cm.

The screen nozzle was designed to replace an array of 2-D grid nozzles mounted in the 2 × 28 cm section. Nominal area ratio 60 orifices were thus selected for comparison purposes and as representative of modern N_2-CO_2 GDLs. Simple 10° conical expansions were chosen based on the results of Sec. II, with a d^* of 0.04 cm selected both to simplify manufacturing and to provide increased $p_o d^*$. Application of a boundary-layer correction (Fig. 1) then gave $d_e = 0.35$ cm. The 2 × 28-cm plate cross section was filled with 6 rows of nozzles, with alternately 79 and 80 nozzles per row. Each nozzle touched its neighbor as can be seen on Fig. 7. The plate was 0.89 cm thick 7075-T6 tempered A1. As the distance from the nozzle throat to the exit plane was 0.77 cm, 0.12 cm was left for the subsonic entry. This was merely drilled through with the throat diameter.

The top and bottom (28 cm wide) walls of the cavity were diverged downstream of the nozzle at an angle of $\frac{1}{2}$° in order to compensate for the calculated turbulent boundary-layer growth. There was an unintentional 0.05 cm gap between these walls and the edge of the nearest row of orifices that created waves in the flow (Sec. IV.A). Opposing 1.5 cm windows were located in the 2 cm walls at stations that were 6, 11, 21, and 31 cm downstream of the nozzle exit. The flow subsequently entered a diffuser and was fed into a dump tank with a volume in excess of 20 times that of the driver.

The collected screen nozzle throat cross-sectional area amounted to only 1% of the cross-sectional area of the 7.5 cm shock tube, so that essentially closed wall reflected shock conditions fed the downstream flow. For the gain studies the shock tube was operated so as to produce nominal values of T_o of 2000 K or 1500 K at a p_o of 50 atm in mixtures of 89% N_2, 10% CO_2, and 1% H_2O by volume. The initial driven tube pressure and the shock velocity were measured for each run and used in an equilibrium real gas calculation of conditions behind the reflected shock. This calculation included the effect of heat

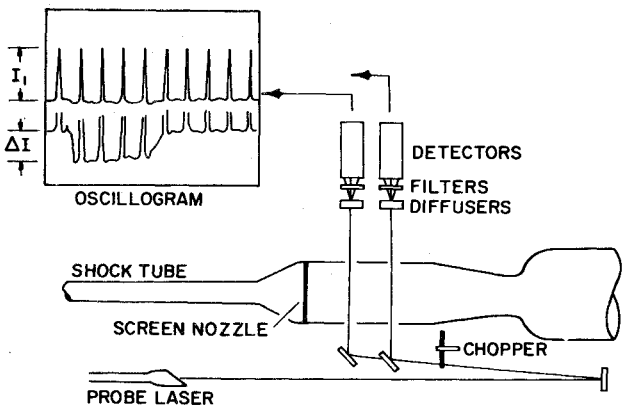

Fig. 8 Gain measuring setup.

addition due to combination of H_2 and O_2 to form the H_2O catalyst. The tube was operated in the tailored-interface mode using He-N_2 mixtures for the driver gas. The reflected shock pressure history was measured just upstream of the screen nozzle for the various run conditions. After starting transients of some $2(10)^{-3}$ sec, it was typically uniform to within $\pm 3\%$ for $7(10)^{-3}$ sec. Earlier line reversal pyrometry measurements showed a temporal drop in T_o, presumably due to losses in the transition section. Therefore all gain readings were taken $4(10)^{-3}$ sec after secondary diaphragm rupture, at which time the nominal 2000 K and 1500 K values of T_o were estimated to have actually been 1750 K and 1300 K, respectively.

The flow quality experiments were run in pure N_2 with a nominal $T_o = 2000$ K and with $p_o = 25$, 50, or 100 atm. The shadowgraphs and interferograms were obtained $6(10)^{-3}$ sec after secondary diaphragm rupture.

B. Flow Quality Instrumentation

Spark shadowgraphs were taken across the flow through the test channel windows. Naturally occurring waves were used to determine the flow Mach number at the 6 and 11 cm stations. However, it was necessary to insert a wedge into the flow in order to obtain sufficient wave structure for this purpose at the 31 cm location.

Double exposure holographic interferometry was the main technique used for the flow quality studies. This is similar to the traditional Mach-Zehnder interferometer, but alignment and component requirements are less stringent. The output from a Q-switched ruby laser ($\lambda = 6943$ Å) was passed through an expanding telescope and then split into two beams. A system of mirrors directed one beam through the test section, the other over the test section, and finally recombined them at a small angle (20°–30°) at the film plate. The optical paths were kept nearly equal. Flow-on and flow-off exposures were made on the film for each experiment. A glass wedge introduced into one of the beams during one of these exposures produced a system of visible fringes in the hologram.

The number of fringe shifts (N) produced on an interferogram by regular density disturbances is readily shown to be given by

$$N = \Delta\phi/2\pi = \beta(L/\lambda)(\rho/\rho_r)(\Delta\rho/\rho) \qquad (7)$$

where β is the density sensitive factor in the index of refraction, referred to a reference density (ρ_r), L is the distance across the flow, λ the wavelength of the radiation, and ρ the density level. $\Delta\rho$ is the average (over L) density difference between two locations in the flow, while $\Delta\phi$ is the phase shift at the interferogram caused by $\Delta\rho$. Equation (7) gives a maximum sensitivity for the present experiments of $\Delta\rho/\rho = 12\%$ per fringe, taking $L = 28$ cm and assuming $A_e/A^* = 60$ nozzles operated with N_2 at $T_o = 2000$ K and $p_o = 100$ atm.

Regular $\Delta\rho/\rho$ patterns should be particularly discernible at high ρ where large fringe shifts occur. However, random disturbances could mix the fringes and destroy the interferogram. The rms value of the fringe shift ($N_{\rm rms}$) obtainable across isotropic turbulence with a Gaussian correlation function can be shown to be[13]

$$N_{\rm rms} = \Delta\phi_{\rm rms}/2\pi = \pi^{1/4}\beta(L/\lambda)(\Lambda/L)^{1/2}(\rho/\rho_r)(\rho'_{\rm rms}/\rho), \qquad (8)$$

where Λ is the characteristic integral scale of the turbulence and $\rho'_{\rm rms}$ the rms-value of the turbulent density fluctuations. Equation (8) may be used to infer $\Lambda^{1/2}\rho'_{\rm rms}/\rho$ from observations of $N_{\rm rms}$. It has been found that $N_{\rm rms} > 0.6$ leads to fringe destruction.[14] This also may be used to obtain $\Lambda^{1/2}\rho'_{\rm rms}/\rho$, if ρ can be raised high enough and if fringe shifts from regular disturbances do not domineer.

C. Gain Instrumentation

The setup used for the gain measurements is shown on Fig. 8. Radiation of 10.6 μ from a 10 W TEM_{00} CO_2 laser was directed by plane mirrors and a beam splitter through KBr test section windows at two locations. The beam was interrupted at a frequency of 500 Hz by a rotating wheel chopper. Apertures of 5-mm removed the wings of the beam, allowing only the maximum energy portion to traverse the test section. After passing through the test section, the beams were diffused by salt-scattering cells. These were viewed through interference filters by Au-Ge detectors. The signals were fed to high gain low-noise amplifiers and then recorded by a pair of dual beam oscilloscopes. As shown on Fig. 8, each output was recorded at two different levels of amplification in order to be able to accurately determine both the initial intensity level (I_1) and the level change (ΔI) at the designated time after secondary diaphragm rupture [$4(10)^{-3}$ sec]. The optical gain per cm (g) was then calculated from $I_1 + \Delta I = I_1 \exp(gL)$, where L is the path length (28 cm) through the active medium. Pure N_2 was used as the test gas for every fourth or fifth run in order to insure that trace deflections were due only to optical gain. These runs indicated a gain uncertainty of 0.04%/cm.

IV. Results and Discussion

A. Flow Quality

The shadowgraphs showed disturbances in the flow at the 6 and 11 cm stations downstream of the screen nozzle. These appeared to be weak shock waves originating at the juncture of the nozzle exit plane with the 28 cm walls, as shown schematically across the top of Fig. 9. Figures 3 and 4 predict an $M_f \approx 5.1$ at $p_o = 50$ atm. The wave angles at the first two stations indicated a rapid decrease in Mach number, with the predicted M_f expected at about 20 cm from the exit plane. The wedge measurements at 31 cm gave an average M that was 3% lower than M_f, suggesting that the last stages of mixing proceed slower.

Both the early wind tunnel screen nozzle[5] and modern 2-D grid nozzle GDL experiments exhibited a final mixed flow that was in general agreement with calculations based on Sec. II.

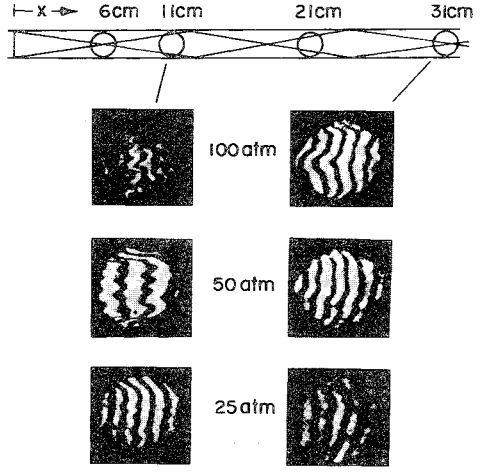

Fig. 9 Interferograms of the flow downstream of the screen nozzle.

Discrepancies might be caused by inlet vena contracta effects on the effective nozzle area ratio, by shock losses within the nozzle core, by existence of a significant base area, and by influence of the cavity walls. The latter can be particularly important in small devices. Without proper boundary-layer correction an effective contraction of the flow cross section would occur which together with the shock system it creates could reduce M significantly. Indications are (i.e., Fig. 9) that the $\frac{1}{2}°$ wall divergence (Section IIIA) satisfactorily minimized these effects in the present experiments, and that the influence of the juncture shock system was at least partially balanced by a higher effective M_e due to the lack of inlet contouring.

Interferograms of the flow at $x = 11$ cm and 31 cm are reproduced on Fig. 9 for the three values of p_o. The wave pattern first indicated by the shadowgraphs can be seen at the highest p_o, while a separate fringe pattern is observable for all of the 11 cm interferograms. This second pattern is particularly clear for $p_o = 50$ atm at 11 cm, where a peak-to-peak average amplitude of ≈ 0.3 fringe is observed in the body of the flow, corresponding to a 7% density nonuniformity (see Sec. III). The peak amplitudes have a separation corresponding to the orifice plate row spacing. Further, they are arrayed in a way suggesting that the disturbances are carried on weak waves at the Mach angle to the flow. Doubling the pressure appears to have doubled the fringe excursions, as would be expected from Eq. (7) (note that the initial fringe spacing on the $p_o = 50$ atm 11 cm interferogram happens to be larger than the rest). Similarly, halving p_o dropped the disturbance to the point where a regular structure of $\approx 0.15\ N$ is barely discernible. Interferograms at the 6 cm station showed a larger regular disturbance, somewhat masked by the strong corner waves, while the 31 cm interferograms can be seen on Fig. 9 to have very little repetitive pattern.

The peak-to-peak amplitude limits of the structured disturbances on the interferograms have been converted to density perturbation, $\Delta\rho/\rho$, through Eq. (7) and plotted on Fig. 5. The corner waves were ignored as far as possible, and the higher pressure runs were preferentially used for maximum accuracy. The density disturbance is seen to decay rapidly with distance downstream. As the interferograms at the first two stations clearly indicated a wave-like character to $\Delta\rho/\rho$, a decay somewhat faster than the 2-D wave line (Eq. 4) on Fig. 5 was to be expected. At some station further downstream, the flow disturbance could still switch over to a 3-D merged wake pattern with a decay faster than that indicated by Eqs. (2) and (3). However, it was not possible to discern which mechanism dominated the downstream flow from the present experiments. An interferogram was taken at the 11 cm station with the optical axis intentionally shifted one orifice spacing in the vertical plane over the cavity width (angle of 0.6°). As expected (Sec. IIC), the regular fringe shift pattern became noticeably more diffuse, indicating an averaging along the optical axis had taken place. The effective integrated $\Delta\rho/\rho$ was reduced by more than a factor of 2.

The $\Delta\rho/\rho$ decay rate of the data on Fig. 5 suggests that randomization to a completely turbulent field has yet to occur at 100 d_s. Nonetheless an upper limit to $\Lambda^{1/2}\rho'_{\text{rms}}/\rho$ can be found from the interferograms. A half-amplitude peak blurring of $\approx 10\%$ of a fringe is seen on the 100 atm 31 cm interferogram of Fig. 9. Approximating N_{rms} as one-third of this, Eq. (8) gives $(\Lambda/d_s)^{1/2}(\rho'_{\text{rms}}/\rho) \approx 3(10)^{-3}$. Thus, the maximum value of ρ'_{rms}/ρ is 10^{-2} for $\Lambda/d_s = 0.1$, dropping to 10^{-3} for $\Lambda/d_s = 10$. The former value of Λ/d_s is characteristic of merged wake turbulence (Sec. IIC). While larger instability-based scales are possible, Fig. 9 is far more suggestive of the wake-like random scale. Note that the indicated maximum $(\Lambda/d_s)^{1/2}\rho'_{\text{rms}}/\rho$ would have to be increased some 20 times before fringe destruction occurred (Sec. IIIB).

Density nonuniformities directly affect the far field intensity of the transmitted beam of radiation. For small phase shifts ($\Delta\phi$) in the exit plane, it can be shown[1] that

$$(I_o - I)/I_o \approx (\Delta\phi)^2 \tag{9}$$

where I_o is the peak beam intensity when $\Delta\phi = 0$, and I the value with distortion. $\Delta\phi$ is given by Eq. (8) for random disturbances,

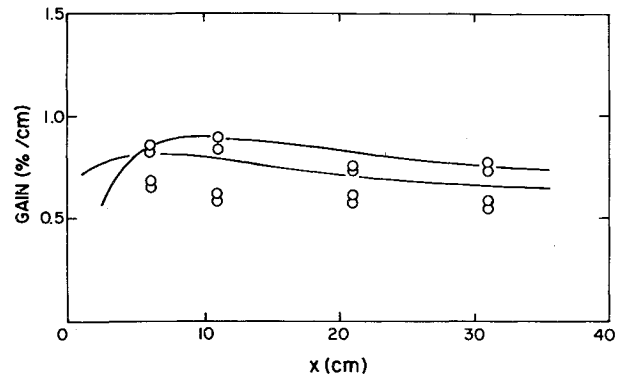

Fig. 10 Gain downstream of screen nozzle (upper data and theory are for $T_o = 1750$ K, lower $T_o = 1300$ K).

and approximately[1] by Eq. (7) for regular ones. With $L = 10$ m, $\lambda = 10.6\ \mu$, $p_o = 50$ atm, $T_o = 2000$ K, and $M_e = 6$, substitution of Eq. (7) in Eq. (9) results in a required $\Delta\rho/\rho \leqq 5(10)^{-3}$ if the peak far field intensity loss is to be kept to 10%. From Fig. 5 this would necessitate setting the cavity up just beyond $x/d_s = 100$. As just discussed, it is also possible to use a nonaligned optical axis at shorter x/d_s. On the other hand, Eq. (8) substituted into Eq. (9) indicates that the maximum value of $(\Lambda/d_s)^{1/2}\rho'_{\text{rms}}/\rho$ assignable to the experiments would cause a nondetectable ($< 10^{-4}$) effect on $(I_o - I)/I_o$ for the representative laser conditions chosen. The reduced relative importance of turbulence occurs because of the $(L)^{1/2}$ dependence of Eq. (8) compared with the direct L dependence of Eq. (7).

B. Kinetic Considerations

Gain data obtained at the four stations downstream of the screen nozzle are collected on Fig. 10. The data are divided into two groups, the upper corresponding to an estimated T_o (Sec. IIIA) of 1750 K, the lower to 1300 K. The symbol size is a measure of the expected experimental uncertainty (Sec. IIIC), and it can be seen that this accuracy assignment is supported by the repeated runs.

Instantaneous mixing model calculations are shown as the solid lines on the figure. This model is seen to give a fair representation of the experimental results for both values of T_o, the agreement being particularly close over the complete downstream history for $T_o = 1750$ K. However, the flow near the exit plane is extremely complex and any agreement in this range must be regarded as fortuitous. Note that the predicted gain at the 31 cm station is 10–15% high for $T_o = 1300$ K. Gain experiments with conventional 2-D grid nozzles run in the same facility produced a similar disagreement with calculation at low T_o. This could be caused by kinetic rate uncertainties, inaccuracies in the catalyst concentration, or by an imprecise T_o correction. The gain vs T_o curves have broad maximums near 1600–1700 K, depending somewhat on x. Thus reducing T_o from a nominal 2000 K to the expected actual value of 1750 K increased the predicted gain by 10–15%, while dropping from 1500 to 1300 K reduced the gain a similar amount.

Note that the high temperature gain on Fig. 10 is larger than that shown on Fig. 6 for 10° nozzles with instantaneous mixing. As just mentioned, some 10% of the difference is due to the higher T_o of Fig. 6. The main difference however, is due to the changed value of $p_o d^*$. The screen nozzle gain of Fig. 10 for which $p_o d^* = 2$ atm cm was found to be 70% of that measured with an equivalent 2-D grid nozzle array at $p_o d^* = 0.8$ atm cm, in agreement with predictions (Sec. IID). The corresponding loss in energy available for lasing was calculated to be only 10%, while the system p_o loss (Sec. IIB) was calculated to actually be smaller for the screen nozzle.

V. Conclusions

The effects of the nonideal flow from GDL nozzles have been analyzed with simple models. The calculations reveal that while

axisymmetric contoured nozzles are unacceptable, moderate angle (10°) conical expansions provide a reasonable compromise between freezing efficiency, boundary-layer losses, and shock losses. Experiments have shown that mixing of the complex exit flow from a screen nozzle comprised of such elements effectively takes place in a downstream distance of 100 element spacings. At this point regular and random density disturbances have decayed to less than 1%. This is in general agreement with both wave-like and wake-like models for the process and is a level that allows high beam quality in a large N_2-CO_2 GDL. The optical gain at this location is accurately predicted by calculations based on the assumption of instantaneous mixing at the nozzle exit.

The calculations show that the performance of the screen nozzle is improved by operating it at a higher $p_o d^*$ than the optimum value for its 2-D counterpart. The over-all pressure recovery of a screen nozzle system may then actually exceed that for the 2-D grid nozzle, while relative gain and laser energy available penalties at least as low as 30% and 10% respectively, can be expected. Performance may be further improved for a specific application through a systematic optimization of screen nozzle geometry, area ratio, gas mixture, optical axis, and operating conditions. Screen nozzles thus offer extreme simplicity and flexibility at little performance cost.

References

[1] Russell, D. A., "Fluid Mechanics of High Power Grid Nozzle Lasers," AIAA Paper 74-223, Washington, D.C., 1974.

[2] Greenberg, R. A., et al., "Rapid Expansion Nozzles for Gas Dynamic Lasers," *AIAA Journal*, Vol. 10, Nov. 1972, pp. 1494–1498.

[3] Director, M. N., "Aerodynamic Parameters Affecting Practical Gas Dynamic Laser Design," AIAA Paper 73-626, Palm Springs, Calif., 1973.

[4] Simons, G. A., "Decay of a Diamond Shock Pattern," *AIAA Journal*, Vol. 10, Aug. 1972, pp. 1037–1043.

[5] Reshotko, E. and Haefeli, R. C., "Investigation of Axially Symmetric and Two-Dimensional Multinozzles for Producing Supersonic Streams," RM E52H28, Oct. 1952, NACA.

[6] Foelsch, K., "The Analytical Design of an Axially-Symmetric Laval Nozzle for a Parallel and Uniform Jet," *Journal of the Aeronautical Sciences*, March, 1949, pp. 161–188.

[7] Cohen, C. B. and Reshotko, E., "The Compressible Laminar Boundary Layer with Heat Transfer and Arbitrary Pressure Gradient," Rept. 1294, 1956, NACA.

[8] Swain, L. M., "On the Turbulent Wake Behind a Body of Revolution," *Proceedings of the Royal Society of London*, Series A, Vol. 125, 1929, pp. 647–659.

[9] Schlichting, H., *Boundary-Layer Theory*, 6th ed., McGraw-Hill, New York, 1968.

[10] Monsler, M. J. and Greenberg, R. A., "The Effects of Boundary Layers on the Gain of a Gas-Dynamic Laser," AIAA Paper 71-24, New York, N.Y., 1971.

[11] Townsend, A. A., *The Structure of Turbulent Shear Flow*, Cambridge University Press, New York, 1956.

[12] Newton, J., Pindroh, A., and Byron, S., "CO_2 Optical Gain in Gasdynamic Lasers Using $CO_2/N_2/H_2O/CO/H_2$ Mixtures," Mathematical Sciences NW, Inc., USAF Rept. AFWL-TR-71-105, July 1971.

[13] Chernov, L. A., *Wave Propagation in a Random Medium*, McGraw-Hill, New York, 1960.

[14] Russell, D. A., Buonadonna, V. R., and Jones, T. G., "Double Expansion Nozzles for Shock Tunnels and Ludwieg Tubes," in *Recent Developments in Shock Tube Research*, edited by Bershader and Griffith, Stanford University Press, 1973.

MAY 1975 AIAA JOURNAL VOL. 13, NO. 5

Shape Change and Conduction for Nosetips at Angle of Attack

JIN H. CHIN*
Lockheed Missiles & Space Co., Inc., Sunnyvale, Calif.

A computerized procedure is developed to determine the three-dimensional thermal response of ablating bodies. The formulation is based upon a spherical, transformed, moving coordinate grid system. An expression for the generalized heat flux for anisotropic media is derived. A lumped capacitance concept is invoked to derive the nodal point heat balance equation. The instantaneous body shape governs the environment predictions. The effects of streamline spreading are taken into account along the windward and leeward rays. The pressure and heat transfer distributions for other azimuthal planes are computed according to a principle of similarity with respect to the local orientation angle. Validating and illustrative results are given. Application of the procedure to graphite nosetip analysis demonstrates that a significant asymmetry is developed in shape and internal temperatures for nosetips at angle of attack.

Nomenclature

a, b, c = principal directions
a_{pq} = $\mathbf{p} \cdot \mathbf{q}$, e.g., $a_{c\xi} = \mathbf{c} \cdot \boldsymbol{\xi}$
A = heat transfer area
c = specific heat
C_H = zero blowing heat transfer coefficient
C_θ = $(\partial r/\partial\theta)_\phi$
C_ϕ = $(\partial r/r \sin\theta\, \partial\phi)_\theta$
Fo = Fourier number
g = h_β/r_c; generalized conductivity, Eq. (7)
G = generalized conductance
h = scale factor for curvilinear coordinate: $h_\xi = \Delta/(1 + C_\theta^2 + C_\phi^2)^{1/2}$, $h_\theta = r$, $h_\phi = r \sin\theta$
h_β = spreading coordinate
k = thermal conductivity
K_1, K_2 = principal curvatures
$\dot{m}_t$ = total mass ablation rate
M = Mach number
p = pressure; index for c, a, b
q = heat flux; index for ξ, θ, ϕ
r = spherical radial coordinate
r_c = cylindrical radial coordinate
r_i = r for inner boundary
r_s = r for nosetip surface
Re = Reynolds number

Presented as Paper 74-516 at the AIAA 7th Fluid and Plasma Dynamics Conference, Palo Alto, California, June 17–19, 1974; submitted June 7, 1974; revision received November 11, 1974. This work was supported by the LMSC Independent Development Program and by Navy Contract N00030-72C-0108.

Index categories: Material Ablation; Heat Conduction; Entry Vehicles and Landers.

* Staff Engineer, Aero-Thermodynamics Department, Engineering Technology. Member AIAA.